ResearchGate

See discussions, stats, and author profiles for this publication at: https://www.researchgate.net/publication/324142023

Droplet splashing on thin moving films at high Weber numbers

Article *in* International Journal of Multiphase Flow · April 2018

DOI: 10.1016/j.ijmultiphaseflow.2018.01.015

CITATIONS
55

READS
346

2 authors, including:

David Burzynski
Coldsense Technologies

9 PUBLICATIONS **203** CITATIONS

SEE PROFILE

All content following this page was uploaded by David Burzynski on 23 July 2019.

The user has requested enhancement of the downloaded file.

International Journal of Multiphase Flow 101 (2018) 202–211

Contents lists available at ScienceDirect

International Journal of Multiphase Flow

journal homepage: www.elsevier.com/locate/ijmulflow

Droplet splashing on thin moving films at high Weber numbers

David A. Burzynski*, Stephan E. Bansmer

Institute of Fluid Mechanics, Technische Universität Braunschweig, Hermann-Blenk-Str. 37, Braunschweig 38108, Germany

ARTICLE INFO

Article history:
Received 20 July 2017
Revised 12 January 2018
Accepted 15 January 2018

Keywords:
Droplet impact
High Weber number
Thin moving films
Thickness measurement
Lamella breakup
Hole formation

ABSTRACT

The influence of a thin moving film on the splashing of droplets was investigated experimentally at high Weber numbers. This study was conducted using a flywheel experiment fitted with a new film generation system, which allows for the production of thin films with variable mean velocity for different liquids. The thickness was measured using a miniature confocal-chromatic sensor during the rotation of the flywheel. Using shadowgraph techniques, the splashing process was analyzed and the evolution of the crown height and diameter were described. It was also demonstrated that the film velocity and thickness influence the development of the crown geometry. The combination of a high-speed and a high-resolution camera allowed us to observe two different instabilities that accelerate the breakup process, leading to a complete atomization of the crown into secondary droplets. The instabilities observed were: spreading holes and a separation from the crown base. Using the formed holes, we calculated the lamella thickness using two different methods, yielding a constant value of 31 ± 3 µm for all the experiments. We estimated both the time at which the hole instabilities appeared and the time at which the breakup process began. Moreover, it was demonstrated that small bubbles in the lamella are responsible for the hole formation. We also showed that the entire breakup process is delayed by increasing the film flow velocity, regardless of the Weber number.

© 2018 The Authors. Published by Elsevier Ltd.
This is an open access article under the CC BY-NC-ND license.
(http://creativecommons.org/licenses/by-nc-nd/4.0/)

1. Introduction

Droplet impact on moving films is a fundamental process in a wide range of technical applications, such as aircraft icing (Liu et al., 2017) and vehicle soiling (Gaylard and Duncan, 2011). When an aircraft flies through a cloud of super-cooled droplets or when a vehicle moves through the rain, droplets impact the surface. A part of the droplet mass that impacts the surface while it is still dry forms a film which sticks to the surface. The other part of the mass atomizes into small secondary droplets. This phenomenon is called splashing. Thereafter, the subsequent droplets impact the thin film directly, and the impact with a dry surface is no longer relevant. The formed thin film then starts to move due to the shear stress on the surfaces caused by the airflow.

The impact dynamics are characterized using the Weber and Reynolds numbers (Josserand and Thoroddsen, 2016). The Weber number (We) is the ratio between the inertial and capillary forces, and the Reynolds number (Re) represents the ratio between the inertial and viscous forces. In the case of droplet impact on wetted surfaces, the film thickness also characterizes the impact dynamics. The film thickness is made dimensionless using the droplet diameter. These characteristic quantities are defined as follows:

$$We = \frac{\rho_l u_{\text{imp}}^2 d_0}{\sigma_{l,g}}, \quad Re = \frac{u_{\text{imp}} d_0}{\nu_l}, \quad \text{and} \quad \delta = \frac{h_f}{d_0}, \tag{1}$$

where ρ_l is the liquid density, d_0 is the droplet diameter, u_{imp} is the impact velocity, $\sigma_{l,g}$ is the liquid surface tension, ν_l is the kinematic viscosity of the liquid, h_f is the film thickness, and δ is the dimensionless film thickness.

Many investigations have been carried out over the last decades in order to better understand the splashing mechanism. Most of them were experimental investigations conducted at relatively low Weber numbers $We < 2,500$, for example Wang and Chen (2000), Rioboo et al. (2003), Hammond et al. (2005) and Deegan et al. (2008). Although these experiments are relevant for many applications — for example, vehicle soiling or aircraft icing where the impact velocities and the droplet diameters are high — the impact may differ in the outcome from the experiments performed at low Weber numbers (see Table 1). An experimental investigation on droplet impacting on a moving film was carried out by Alghoul et al. (2011) at $We < 460$ and $\delta > 1$. They observed that the shape of the jets were firstly asymmetric but became more symmetrical over time. However, the Weber numbers and film

* Corresponding author.
E-mail address: d.burzynski@tu-bs.de (D.A. Burzynski).

https://doi.org/10.1016/j.ijmultiphaseflow.2018.01.015
0301-9322/© 2018 The Authors. Published by Elsevier Ltd. This is an open access article under the CC BY-NC-ND license. (http://creativecommons.org/licenses/by-nc-nd/4.0/)

thicknesses do not correspond with vehicle soiling or aircraft icing problems. One of the few experimental investigations at $We > 3000$ and $\delta > 1$ was performed by Pan et al. (2008). They observed that different crown forms can be generated by changing the thickness of the film. However, the film was not moving in those experiments and higher Weber numbers were not achieved. This restriction on Weber number variation was due to a breakup process caused by aerodynamic drag on the droplets and oscillation during the cutting process. More recently, Faßmann (2015) managed to overcome the breakup process by accelerating the substrate instead of the droplets. He carried out a statistical investigation to quantify the diameter and velocities of the secondary droplets at $We = 700$ and $We = 3500$, with varying film thickness of $\delta > 0.1$. This experiment resulted in the conclusion that an increase in Weber number causes a reduction in diameter size of the secondary droplets, but increases the quantity of small droplets.

Table 1
Examples of Weber numbers presented in aircraft icing and vehicle soiling problems (see Bringi et al. (2003) and EASA CS-25 (2009)).

Example	d_0 (μm)	u_{imp} (m/s)	We
Vehicle soiling	100–4000	3–33	12.4–59,876
Aircraft icing	15–50	60–120	742–9897

The time evolution of splashing and the formation of the secondary droplets have also been studied by many authors. One of the most important works was performed by Cossali et al. (1997). They observed the droplet impact at low Weber numbers and categorized time evolution in four different phases: (1) the formation of the crown and possible prompt splash, (2) the instability of the rim and jet formation, (3) the breakup of jets and the formation of secondary droplets, and (4) the period of crown collapse. A later work presented by Thoroddsen (2002) showed that an axisymmetric ejecta sheet arises before the crown is formed at $\delta > 0.5$, i.e., during the first phase described by Cossali et al. (1997). This ejecta sheet disintegrates when $We > 500$ and generates secondary droplets, which should not be confused with the secondary droplets generated by the crown (Zhang et al., 2010). Afterwards, Zhang et al. (2012) demonstrated that the size of these secondary droplets is not necessarily much smaller than the size of the droplets generated by the crown, and that no correlation exists between the droplet origin and droplet size. The breakup mechanism that causes these secondary droplets has been studied by many authors, as shown in Dhiman and Chandra (2010). One interesting observation was made by Wang and Chen (2000), who found that the crown breakup starts from the lower part of the crown, when droplets impact very thin fluid films. However, those observations were made at very low Reynolds numbers ($Re = 1168$), and are not provided as a detailed time-resolved visualization. In the aircraft icing and vehicle soiling problems, the Reynolds number is one order of magnitude higher.

More recently, Roisman et al. (2006) performed a linear stability analysis showing that the main source of secondary droplets is the creation and breakup of the crown. This phenomenon is similar to the bag breakup process caused by the aerodynamic drop deformation, as shown in Opfer et al. (2014). A different breakup mechanism was observed by Thoroddsen et al. (2006) using a film of lower surface tension than the primary droplet. This kind of splashing produces small droplets from the film, which impact with the inner side of the lamella, subsequently generating holes. However, when the primary droplet and the film have the same surface tension, the lamella does not breakup by hole formation. Studies on the rupture of thin soap films have been carried out for the last decades showing a similar behavior regarding the hole formations in the lamella (Taylor, 1959; Culick, 1960; Prévost and Gallez, 1986; Thete et al., 2015). The rupture characteristics and the thickness evolution of such films is described by a nonlinear theory, characterizing the surface waves, as shown in Prévost and Gallez (1986).

In contrast to the large number of experiments on droplet impacts performed to date, only a few theoretical investigations have been carried out (Josserand and Thoroddsen, 2016). One notable theory was presented by Yarin and Weiss (1995). They developed a mathematical model for the description of the splashing phenomena which is based on a kinematic discontinuity in the velocity. This model is in agreement with the experiments at low Weber numbers. Later, Roisman and Tropea (2002) generalized this theory for the impact on liquid fluids and inclined surfaces. As with the theory of Yarin and Weiss (1995), the generalization performed by Roisman and Tropea (2002) is also in agreement with the experiments. However, this model has not been validated at high Weber numbers due to missing experimental data. A review of the recent theoretical, numerical, and experimental investigations of droplets impacting with a solid and wetted surface can be found in Yarin (2006), Thoroddsen et al. (2008), and Josserand and Thoroddsen (2016).

In this study, we aim to describe the splashing of monodispersed droplets on thin moving films ($\delta < 0.15$) at high Weber numbers ($We > 2000$). Specifically, we seek to observe the splashing and describe the formed crown and lamella thickness, and compare it with the four phases of splashing at low Weber numbers presented by Cossali et al. (1997). We also intend to describe the influence of the film velocity on the crown geometry and on the breakup process. This work aims to give us further insight into the splashing phenomenon on moving films at high Weber numbers by providing a detailed description of various crown geometries and the breakup process, which is relevant for a host of technical applications.

2. Experimental methods

We redesigned the flywheel experiment introduced in Faßmann et al. (2013) to achieve high Weber numbers and reproduce the impact of monodisperse droplets normal to thin moving films. Moreover, we developed a new film generation system which allowed for the investigation of moving films of different fluids — such as water or alcohols — to be conducted (see Fig. 1(a)).

The mode of operation of the flywheel experiment can be described as follows: Each droplet is formed and released by a droplet generator. These droplets fall freely due to gravity through a shielding tube. Meanwhile, the flywheel, on which the substrate is mounted, rotates under the droplet generator at a constant angular velocity (ω).

The droplet generator consists of a syringe pump, a needle, a polyurethane hose, and a cage with a solenoid (see Fig. 1(b)). The syringe pump KDS200 from KD Scientific was used to regulate the volume rate. The syringe is connected to the needle under the cage through the polyurethane hose. After a specific amount of water is pumped into the needle, the droplet forms and hangs until the cage is hit by the solenoid. Subsequently, the droplet separates itself from the needle and falls under the influence of gravity. The flywheel and the droplet generator are synchronized so that droplets impact on the substrate surface after some milliseconds of free fall. A Standford DG535 delay generator was used to synchronize the droplet generator and cameras to the flywheel. To investigate the impact of droplets on wetted surfaces, a thin moving film is generated on the substrate during the rotation of the flywheel. This is done using a recirculation system that pumps fluid into the flywheel.

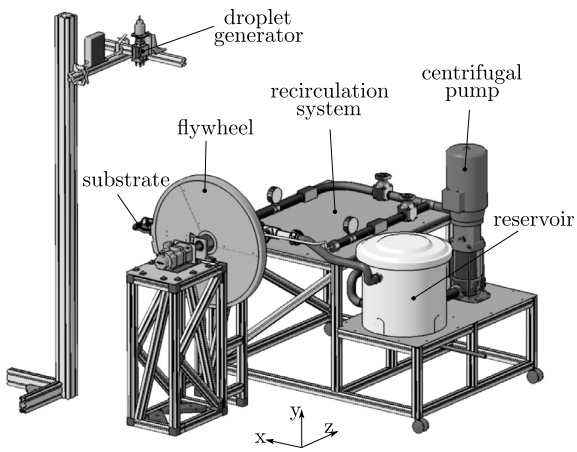

(a) Overview of the flywheel experiment.

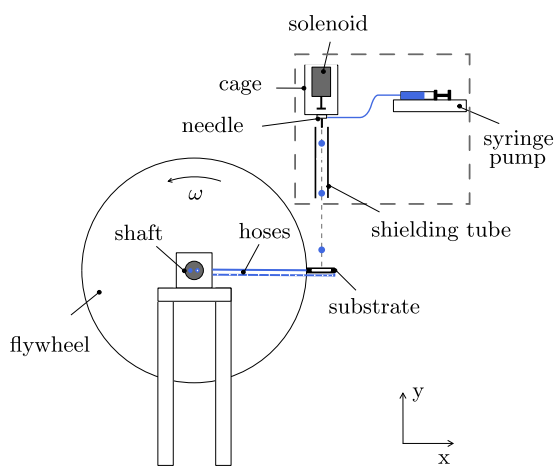

(b) Schematic representation of the flywheel and droplet generator (gray dashed box).

Fig. 1. Setup of the flywheel experiment. The droplets are formed by the droplet generator while the flywheel and the substrate rotate at a constant angular velocity. The recirculation system pumps and extracts the liquid into and from the flywheel to generate a thin fluid film.

2.1. The film generation system

The generation of a thin moving film on a rotary system is a very challenging task. On one hand, the fluid has to be provided continuously from the outside of the flywheel to the substrate. On the other hand, the film has to be extracted from the flywheel to avoid splashing of the liquid on the measurement equipment. Additionally, if the extraction does not take place, the distinction between the secondary droplets and the film scattered all around by the flywheel cannot be made. For this reason, we designed a recirculation system that performs both the injection and the extraction.

Basically, the fluid is stored in the recirculation system and is then pumped out through the flywheel shaft to the substrate. At the substrate, the fluid film is generated. Afterwards, it is extracted to the recirculation system, closing the loop (see Fig. 2).

2.1.1. The recirculation system

The liquid in the 40-l reservoir is pumped out by a centrifugal pump and divided into two subsystems (see Fig. 2(a)). One of these subsystems transports the fluid directly into the flywheel $\dot{Q}_{in}$. Before it enters the flywheel, the flow rate ($\dot{Q}$) and the pressure are measured to control the conditions of the fluid. A diaphragm valve attached to the measurement equipment allows for regulation of the flow rate into the flywheel. Note that by measuring and regulating the flow rate, it was possible to set the mean velocity of the film on the substrate due to mass conservation $\overline{u_f} = \dot{Q}_{in}/A$, where A represents the nozzle exit area.

The other subsystem activated the ejector $\dot{Q}_{ej}$, which continuously extracted the water–air mixture from the suction chamber at the substrate $\dot{Q}_{out}$. As in the first subsystem, the measurement of the flow rate and pressure — together with the regulation of the flow rate using a diaphragm valve — allowed us to control the suction power and the ejector. Note that the amount of liquid that exited the ejector is equal to $\dot{Q}_{out} + \dot{Q}_{ej}$. This liquid flow was then transported directly to the reservoir to close the loop. We also installed a pressure regulator as a bypass in order to establish optimal conditions in the flow before it enters the two subsystems.

2.1.2. The flywheel shaft

The flywheel provided an increase in impact velocity, which results in the ability to achieve relatively high Weber numbers. Simultaneously, the flywheel shaft allows the transfer of fluids to and from the substrate. The fluid transfer was facilitated using two shafts: one rotary shaft that connects the flywheel to the motor, and a second that is fixed to the frame (see Fig. 2(b)). The fluid coming from the recirculation system $\dot{Q}_{in}$ enters the fixed frame and fills an external circular channel, while a drill-hole in the rotary shaft with access to the same filled channel transports the fluid to the substrate. An identical design but in another channel transports the fluid in the other direction $\dot{Q}_{out}$. Both channels are separated by o-rings to prevent the flows from mixing. The advantage of this design is that not only is the transport of the fluid possible, but also that optical and electrical signals are able to be transferred into the rotating flywheel. In our configuration, we used a SRG12 fiber optic rotary joint (FORJ) from Princetel in the fixed shaft in order to transmit all optical and electrical signals to the sensor.

2.1.3. The substrate and film thickness measurement

The liquid coming through the shafts $\dot{Q}_{in}$ is accelerated by a nozzle onto the substrate, generating a thin fluid film (see Fig. 2(c)). This thin film went through our observation window, and then ended up in a suction chamber where it got mixed with the surrounding air. From this suction chamber, the water–air mixture $\dot{Q}_{out}$ is sucked by the lower pressure generated by the ejector in the recirculation system. The water–air mixture goes trough the shafts and ends up in the reservoir, closing the film generation loop.

The thickness of the film on the substrate is measured using a confocal chromatic measurement system from Micro-Epsilon. This system consists of an IFC2451 controller and an IFS2902/90-4 miniature sensor model, which is mounted under the substrate as shown in Fig. 2(c). The controller generates a polychromatic white light, which is sent to and returned from the sensor. Inside this sensor, a combination of lenses disperses the light such that different wavelengths are focused at different distances from the sensor head. The distance from an interface to the sensor is determined by the reflected wavelength. This method allows the thickness of transparent materials and liquids to be measured. The white light is transferred from the controller to the sensor and vice versa through the FORJ mounted on the fixed shaft. This approach allows us to measure and control the thickness of the film during the experiments involving the rotation of the flywheel.

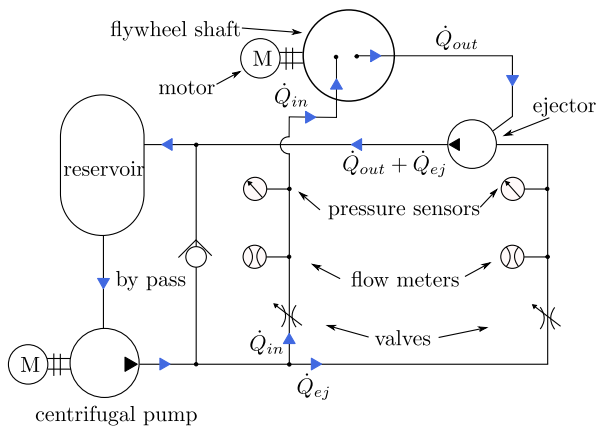

(a) The recirculation system: A centrifugal pump generates a constant flow rate transporting the liquid into the flywheel $\dot{Q}_{in}$ and starting the ejector $\dot{Q}_{ej}$.

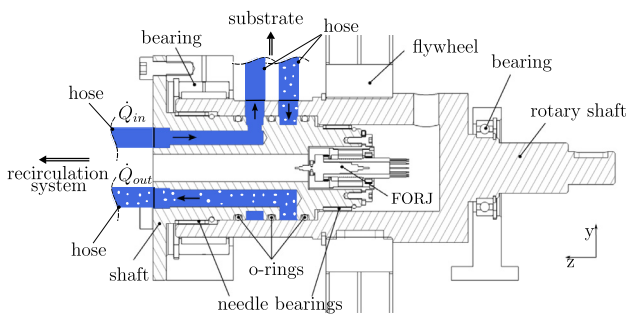

(b) The flywheel shaft: It transfers the liquid from the recirculation system $\dot{Q}_{in}$ to the rotating substrate and vice versa $\dot{Q}_{out}$. Additionally, a FORJ transfers electrical and optical signals to the substrate.

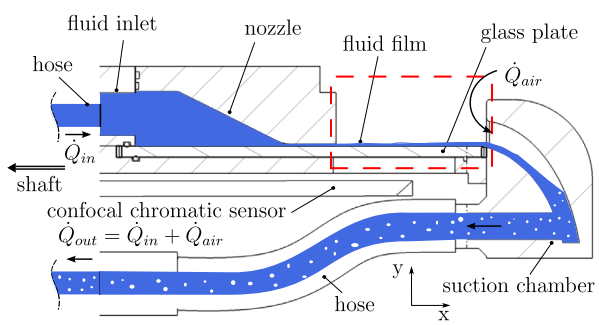

(c) The substrate: A nozzle forms the thin fluid film, which later on is extracted from the suction chamber. The film thickness is measured using a confocal chromatic sensor.

Fig. 2. The film generation system.

2.2. Observation methods

To observe the time evolution of the quick splashing process, we used a shadowgraph technique with a Shimadzu HPV-2 high-speed camera and two different objectives: a 180 mm Tamron objective with a 2× teleconverter and a Questar QM 100 long-distance microscope (see Fig. 3). The observation window is illustrated in Fig. 2(c) as a dashed square. This observation window is illuminated by a conventional halogen lamp.

Even through the long distance microscope maximizes the field of view drastically, a host of details remains unobserved due to the poor resolution of the high-speed camera of 312 × 260 pixel. A double-frame CCD camera PCO.4000 from PCO AG with a resolution of 4008 × 2672 pixel together with a Nd:YAG nanoPIV laser with diffuser optics from LaVision GmbH is used to observe the lamella in detail. Since the PCO.4000 has a low frame rate, it captures only two pictures during the entire splashing process. The time when the droplet first impacts with the film can therefore not be determined directly from these two frames. Instead, as described in Section 4.2, the shape of the crown is used to reconstruct the elapsed time (t).

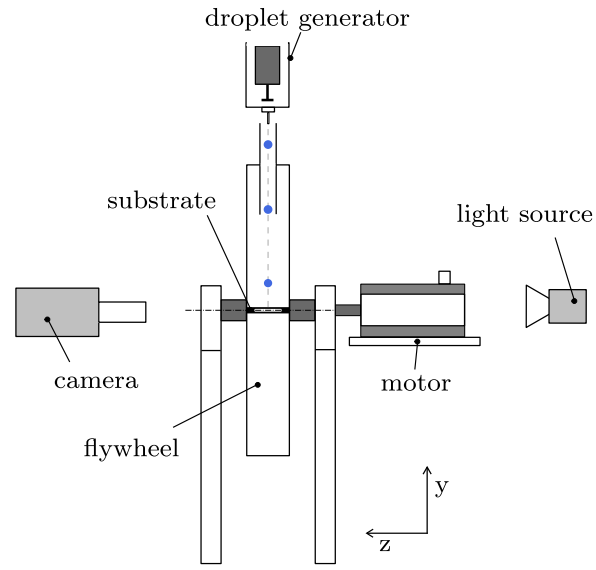

Fig. 3. Observation methods: the splashing was recorded with a Shimadzu HPV-2 high-speed camera and a double-frame PCO.4000 high-resolution camera using shadowgraph techniques.

2.3. Characterization of the experiments

This study concentrates on the perpendicular impact of monodispersed distilled water droplets on thin moving films of the same fluid at high Weber numbers. The velocity of this thin fluid film and the Weber number are systematically varied to investigate their influence on the crown geometry and on the breakup process. While the film velocity is set by changing $\dot{Q}_{in}$, the desired high Weber number is achieved by adjusting the angular velocity of the flywheel exclusively. Note that the impact velocity used in the Weber number is the relative velocity between falling droplet and rotating substrate. A smooth glass plate (roughness average $R_a = 11$ nm and roughness mean peak to valley height $R_z = 608$ nm) is required as a substrate to allow the measurement of the film thickness using the confocal-chromatic sensor, as explained in Section 2.1.3. These measurements showed that the film thickness varies depending on the angular velocity and position of the flywheel due to forces acting on the film, such as gravity and centrifugal force. Keeping the flow rate ($\dot{Q}_{in}$) constant and varying the angular velocity leads to an inevitable variation in the film thickness for different angular velocities. As a result, we investigated six different setups for this study at ambient conditions (temperature $T = 19.3 \pm 0.4$ °C and pressure $p = 1013.4 \pm 1.2$ hPa), as shown in Table 2. We recorded over a thousand splashes of each setup with both cameras for a total of 4335 videos and images.

In order to compare the splash evolution between the different setups from Table 2, we set $t = 0$ when the droplet first impacted with the film. As shown in Fig. 4(b), this moment was determined manually for each impacted droplet when the background light between the droplet and the film was no more visible. Due to the observed quick splash process, we defined an uncertainty of ±1

Table 2
Summary of setups and dimensionless parameters used in the experiments.

No.	1	2	3	4	5	6
d_0 (mm)		3.00 ± 0.12			3.00 ± 0.12	
u_{imp} (m/s)		7.44 ± 0.03			10.53 ± 0.03	
We (–)		2281 ± 180			4569 ± 317	
Re (–)		20,596 ± 1293			29,113 ± 1692	
u^* (–)	0.05 ± 0.005	0.15 ± 0.006	0.29 ± 0.008	0.04 ± 0.008	0.10 ± 0.008	0.20 ± 0.006
δ (–)	0.05 ± 0.02	0.13 ± 0.01	0.14 ± 0.01	≈0.03	0.04 ± 0.02	0.05 ± 0.02

frame, when the droplet first impacted with the film. The recording rate of the camera was 16,000 fps at $We = 2281$ and 32,000 fps at $We = 4569$, leading to a time uncertainty between frames of ±62.5 µs and ±31.3 µs respectively. Moreover, the elapsed time was made dimensionless using the impact velocity and the droplet diameter ($\tau = tu_{imp}/d_0$). Note that the uncertainty in the determination of the elapsed time is the dominant contributor to the values of τ in the results. In addition to the dimensionless parameters presented in Section 1, the following factors are used to compare the different impacts listed in Table 2:

$$H_c = \frac{h_c}{d_0}, \quad D_c = \frac{d_c}{d_0}, \quad u^* = \frac{\overline{u_f}}{u_{imp}}, \quad \tau = \frac{tu_{imp}}{d_0} \tag{2}$$

where H_c is the dimensionless crown height, h_c is the crown height, D_c is the dimensionless crown diameter, d_c is the crown diameter, u^* is the dimensionless film velocity, and τ is the dimensionless time.

3. Observation of impact

Our observations revealed that the crown shape changed its slope over time, as shown in Fig. 4. In the early phase of splashing ($\tau < 1$) the shape was almost symmetric regardless of the Weber number or film thickness. Shortly after, the upstream side of the crown (left side in images) is strongly influenced by the film velocity because the spreading velocity of the droplet and the film develop in opposite directions. On the downstream side (right side in images), the crown developed more perpendicularly to the film (see Fig. 4(d)). Later, when the splashing process was in the development phase ($2 < \tau < 5$), the curvature of both crown sides increased. The curvature variation in the upstream side was almost negligible but still noticeable, while the curvature of the downstream side varied drastically (see Fig. 4(e)–(h)). After the development phase ($\tau > 5$), the curvature on the downstream side decreased gradually and the crown became more perpendicular to the film flow. This final symmetrical development over time agrees with the jets observations made by Alghoul et al. (2011) on moving pools at much lower Weber numbers ($We < 460$), suggesting that the final symmetrical development is an universal phenomenon.

Moreover, we demonstrated that the crown shape depends on the film velocity during the development phase, see Fig. 5. When the film velocity $u^* = \overline{u_f}/u_{imp}$ was smaller than 0.05, an almost symmetric shape was formed. This occurred because the inertial forces of the droplet were much greater than the inertial forces of the film flow, and therefore, the almost symmetric shape was similar to the observation of droplet impacts on films at rest. As expected, an increase of the film velocity reduced the ratio between both inertial forces, and the film flow influenced the crown formation generating a curved lamella (see Fig. 5). This effect became more noticeable when the film velocity was greater than 2 m/s ($u^* > 0.29$). At such high film velocities, the film flow additionally translated the entire crown base in the flow direction.

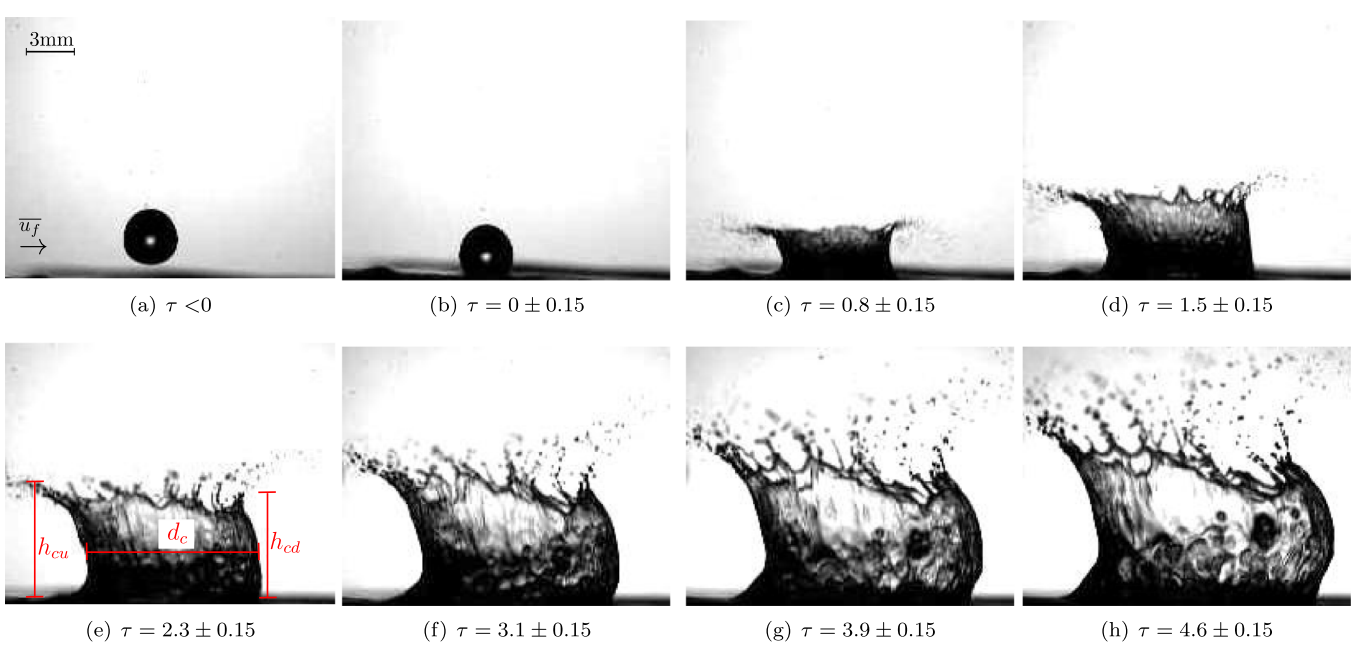

(a) $\tau < 0$ (b) $\tau = 0 \pm 0.15$ (c) $\tau = 0.8 \pm 0.15$ (d) $\tau = 1.5 \pm 0.15$

(e) $\tau = 2.3 \pm 0.15$ (f) $\tau = 3.1 \pm 0.15$ (g) $\tau = 3.9 \pm 0.15$ (h) $\tau = 4.6 \pm 0.15$

Fig. 4. Evolution of a droplet splashing onto a moving film for $u^* = 0.15$, $\delta = 0.13$ at $We = 2281$. The curved crown shape is the result of the thin moving film. See also supplemental video 1. (e) shows how the crown diameter and height were measured.

(a) $u^* = 0.05$ (b) $u^* = 0.15$ (c) $u^* = 0.29$

Fig. 5. Film flow effects on the crown geometry at constants $We = 2281$ and $\tau = 4.6$. At flow velocities lower than 5% of the impact velocity, the crown shape remains symmetric. At higher velocities, the crown deflects. This deflection increases along with increasing film velocities.

4. Results and discussion

4.1. Crown geometry

The effects of impact velocity and film flow on the crown shape are quantified measuring the crown diameter and height over time. The diameter d_c is evaluated approximately at the middle of the crown, while the crown height h_c is obtained by taking the average between the upstream (h_{cu}) and downstream side (h_{cd}), as shown in Fig. 4(e). These values are made dimensionless using the primary droplet diameter d_0, as explained in Section 2.3. Later on, in Section 4.2, we will use the gathered temporal evolution of the crown shape to reconstruct the dimensionless time τ of the high resolution images that documents the crown breakup.

Fig. 6 shows the crown diameter evolution for different Weber numbers and film velocities. During the early phase of impact ($\tau < 2$), the diameter developed similar in all cases regardless of the Weber number and film velocity. However, during later stage for $\tau > 5$, the crown diameter became larger with increasing Weber numbers. The reason is that the higher inertial force of the droplet intensifies the expansion of the crown, leading to a larger diameter. Furthermore, the influence of the film properties is recognizable. With the simultaneous increase in film velocity and, therefore, an inevitable increment in the film thickness (see again the detailed parameters in Table 2 and clarification in Section 2.3) the dimensionless crown diameter decreased. This is due to the higher inertial forces of the film, which alter the spreading process.

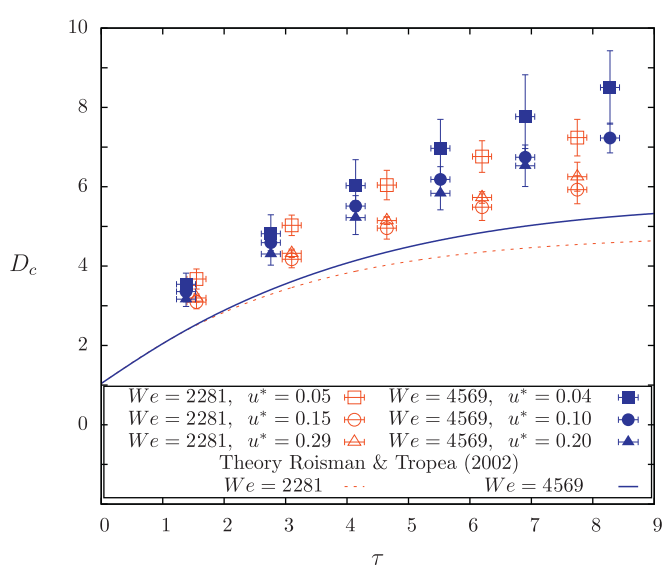

Fig. 6. Time development of the dimensionless crown diameter of all experiments setups. An increment of the film velocity over 10% of the impact velocity ($u^* > 0.1$) leads to a reduction of the crown diameter regardless of the Weber number.

Our measurement results were compared with a theoretical model presented by Roisman and Tropea (2002), where the crown geometry is described from a kinematic point of view for inclined fluid films at rest. This model tends to underestimate the measured diameter for all the studied Weber numbers. The difference between model and measured diameters at $\tau > 7$ and for $We = 4569$ was about 44%, however the prediction at lower Weber numbers is more accurate. One of the reasons for such inaccuracy might be the assumptions made by Roisman and Tropea (2002). They argued that if the impact velocities are as high as in our experiments, the inertial forces before the droplet impacts with the surface ($\rho u_{\text{imp}}^2 d^2 = 4.9 \times 10^{-1}$ N) are more dominant than the small forces of surface tension ($\sigma d = 2.2 \times 10^{-4}$ N) and viscosity ($\mu u_{\text{imp}} d = 2.2 \times 10^{-8}$ N). They concluded therefore that the effects of surface tension and viscosity can be neglected; however, this assumption is only true in the early stage of impact. When the droplet spreads across the film at $\tau > 0$, the friction between it and the film yields to a reduction of the inertial forces; consequently, the surface tension and viscosity effects become more important. Another reason may be that the theoretical model ignores the effects of the surrounding air, which also influence the splashing outcome as shown in Josserand and Thoroddsen (2016)). As a consequence of our observations, all these effects should be taken into consideration in the development of future models even if the inertial forces are much higher than the surface tension or viscosity.

Fig. 7 illustrates the evolution of the mean crown height over time. Note that the crown height is obtained measuring the upstream and downstream side height and taking the mean of both values. Our observations demonstrated that the breakup process played a fundamental role in the development of the crown height, leading to different observations depending on the impact and film velocity. When the droplet impacted at $We = 2281$, an increase in the film velocity resulted in a smaller crown height on the downstream side due to the crown curvature (see Fig. 5). Even though this effect was notable, the mean height, which is plotted in Fig. 7, stayed at a constant value irrespective of the film velocity. This phenomenon occurred only until $\tau \approx 6$, whereafter the formed crown for the lowest film velocity ($u^* = 0.05$) broke up and the measured crown height started to decrease (see Fig. 7). This indicates that the thick moving film supplies the crown with more liquid, delaying the breakup process; therefore, the higher the film velocity and thickness, the later the breakup begins.

Indeed, our observations showed that the breakup processes always started first on the downstream side, where no fluid film flow stimulates the crown formation (see Fig. 8). Moreover, for $We = 4569$, the crown broke up even earlier, which resulted in even smaller dimensionless crown heights compared to the case of small Weber number. Regarding the model developed by Roisman and Tropea (2002), the crown height seems to be

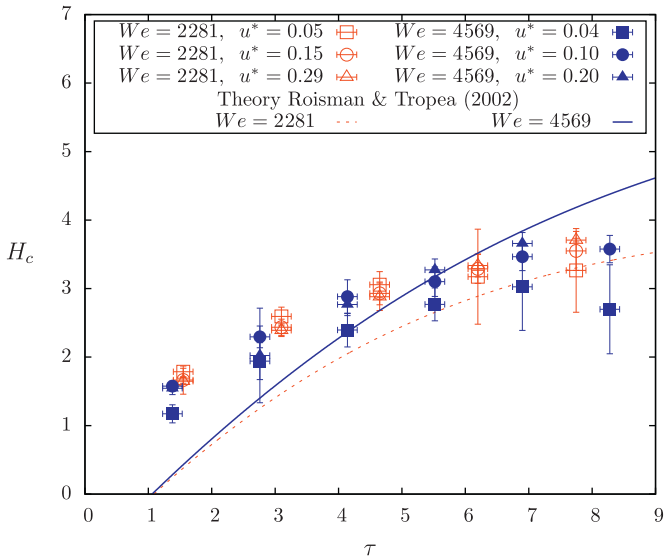

Fig. 7. Time development of the mean dimensionless crown height of all experiments setups. The mean crown height slightly decreases by an increment of the film velocity at $We = 2281$ and $\tau < 5$. On the contrary, it increases with the film velocity at $We = 4569$.

underestimated at the early phase ($\tau < 5$) but overestimated at later times, about 40% at $We = 4569$ and $u^* = 0.04$. On the contrary, for $We = 2281$ the model always underestimates the crown height.

4.2. Crown breakup

We observed that the crown completely destroys itself in the last phase of splashing due to two different types of instabilities (see Fig. 8). The first instability consisted of holes formed typically in the middle of the crown, which spread throughout the lamella until the crown rim or base is reached. A similar breakup process was observed in thin soap films after puncturing (see Taylor, 1959; Culick, 1960), and in the splashing of droplets using a film of lower surface tension than the primary droplet (see Thoroddsen et al., 2006). Recently, Marston et al. (2016) observed the hole formation near the crown top using a solid sphere as an impact object onto deep pools at high Weber numbers. However, this hole formation was not expected for droplets and films of the same fluid as in our investigation. This process is analyzed in detail later in this section.

The second instability was the separation of the lamella from the crown base, which is reported in Wang and Chen (2000) for droplet impact on thin film layers and at low Weber and Reynolds numbers. Even through these different breakup processes have been observed separately and are the results of different setups,

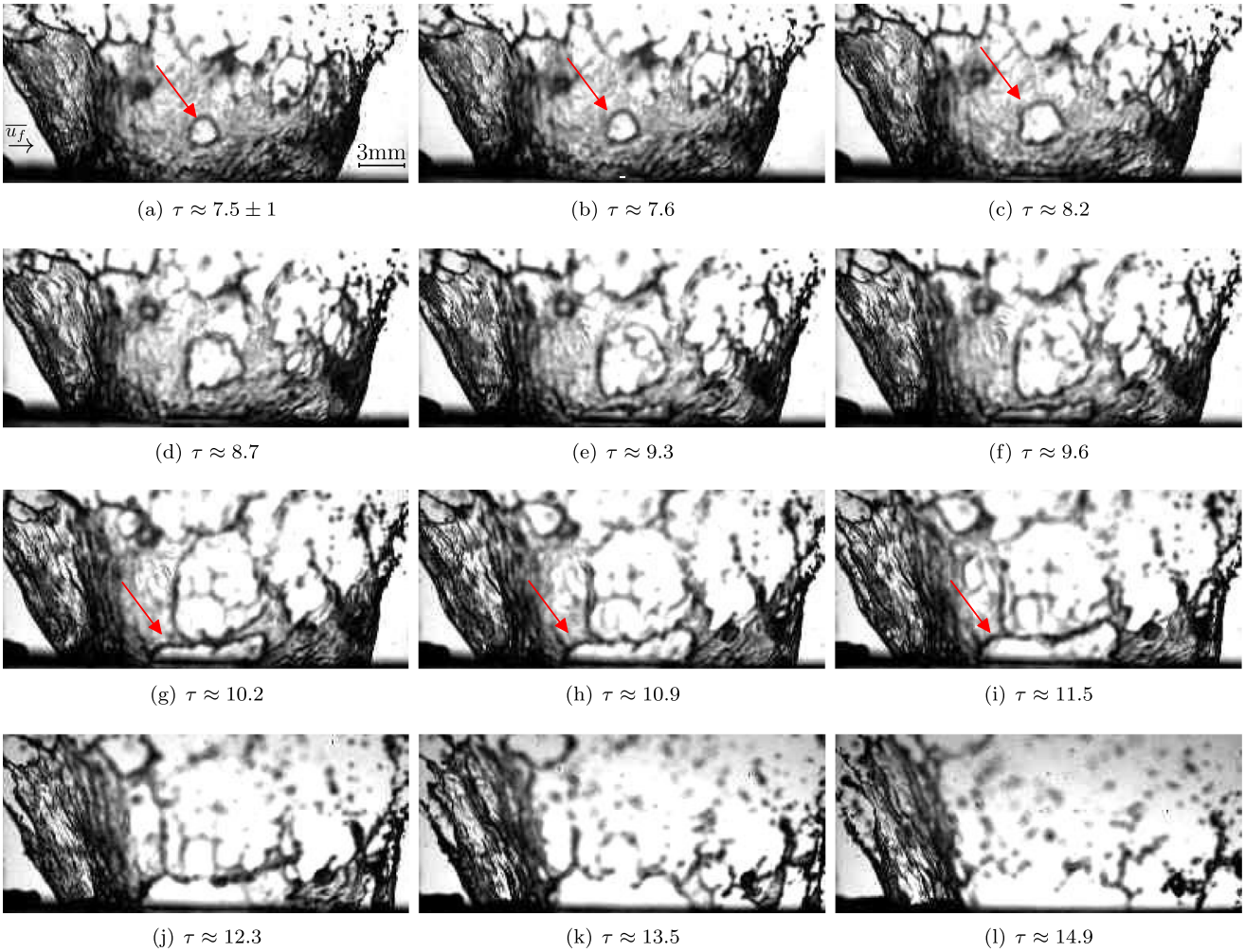

Fig. 8. Crown breakup process at high Weber numbers ($We = 4569$ and $u^* = 0.04$). The film flows from left to right. The arrow shows the rims generated in the breakup phase for the hole formation and the separation from the base. See also supplemental video 2.

Fig. 9. Droplet impact at 15.2 m/s ($We = 9500$) on a thin moving film ($\delta \approx 0.05$, $u^* = 0.1$). The impact outcome became chaotic and a measurement of the crown geometry was not possible.

our experimental investigations demonstrated that both instabilities are present in the same splash at high Weber and Reynolds numbers (see Fig. 8). Additionally, this separation from the crown base occurred first on the sides or downstream but never upstream, while the holes were formed all around the crown. Considering this fact, it is clear that the moving film affects this instability, delaying the phenomenon upstream due to the constant mass supply into the crown. This process was observed in all experiments; however, the smaller the film velocity and thickness, the earlier occurs the separation. As a consequence of these instabilities, the entire crown atomizes into secondary droplets, and, unlike in the description of Cossali et al. (1997), its collapse was not observed.

Regarding the time when these instabilities appeared, we observed that the hole formation started at $\tau \approx 7 \pm 0.5$ in all experiments at a film velocity smaller than 5% of the impact velocity, while the separation of the base began at $\tau \approx 8 \pm 0.5$. Keep in mind that our method to calculate the impact time and its uncertainty, as explained in Section 2.3, is also crucial in the definition of τ. The hole formation and the separation threshold time was affected by the film velocity, thereby retarding the breakup process when the film velocity was increased. For film velocities higher than 10% of the impact velocity, the hole formation and the separation of the base started at $\tau \approx 8 \pm 0.5$ and $\tau \approx 9 \pm 0.5$ respectively. In this later phase $\tau > 7$, the crown height remained almost constant, indicating the growth limit of the crown (see Fig. 7).

We attempted to investigate the impact at even higher Weber numbers ($We = 9500$). However, a quantification of the crown geometry—as performed for $We = 2281$ and $We = 4569$—was not achievable due to the very chaotic crown shape (see Fig. 9). The required angular velocity of the flywheel was too high for the generation of a laminar fluid flow at the substrate surface, and therefore, the crown shape became irregular and chaotic. Further investigation using a different fluid of lower surface tension, density, and viscosity would help to solve this problem. The idea is to reduce the required angular velocity of the flywheel using e.g. ethanol as droplet fluid and maintaining the same diameter of 3.0 mm. This would reduce the necessary angular velocity by half.

We observe the hole formation in detail using the high-resolution camera in order to describe its characteristics. Since this camera takes only two pictures for each impact, we calculate the elapsed time measuring the diameter and height of the observed splash. The uncertainty obtained by the calculation of the elapsed time from the high-speed camera, as explained in Section 4.1, propagates also to this analysis. Fig. 10(a) shows the high-resolution image of the forming hole at $\tau \approx 7.5 \pm 0.5$, demonstrating that it is surrounded by waves of different wavelengths and amplitudes. Due to the fact that the holes appeared at different azimuthal positions, the images were corrected to eliminate the perspective distortion for those holes located downstream and upstream from the crown center. The correction was made by defining the crown arc ($s = R \cdot \arcsin(x/R)$) as the new and transformed horizontal axis, where R is the crown radius. This transformation unfolds the cylindrical shape of the crown into a 2D SY-plane as shown in Fig. 10(a). The intensity values of each pixel

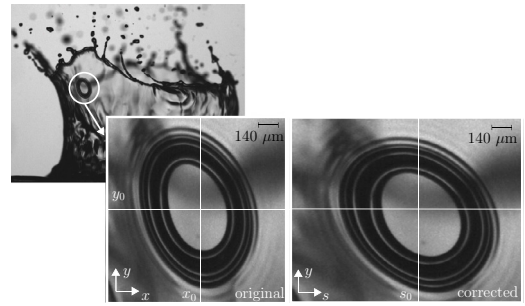

(a) Hole in the lamella, which is identified in the high-resolution camera. The first zoomed image shows the original crop, while the second shows the corrected image.

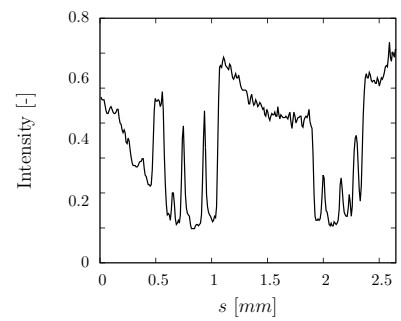

(b) Light intensity signal of the corrected image (a) at y_0.

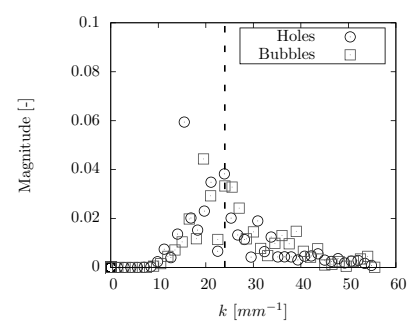

(c) Power Spectral Density

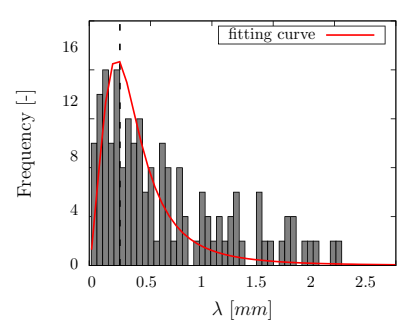

(d) Histogram of wavelength with a log-normal distribution curve.

Fig. 10. Analysis of the holes and bubbles in the lamella during the breakup process $\tau > 7$.

in the transformed plane were obtained using a shape-preserving piecewise cubic interpolation. This kind of image is analyzed later by obtaining the light intensity signal for a constant vertical and horizontal direction, y_0 and x_0 or s_0 respectively (see Fig. 10(b)).

Later, a discrete Fourier transform (DFT) is performed for these signals, obtaining the oscillatory components of the waves around the holes (see Fig. 10(c)). Additionally, the wavelengths are calculated by setting an intensity threshold from 70% of the brightest pixel signal and measuring the lengths between the detected shadows (see Fig. 10(d)). We observed that the location of the shadows varied depending on the setting of the intensity threshold. In our case, the 70% threshold leaded to an uncertainty of around 6 pixel (54 µm). Both the spectral density and the wavelength histogram show a local maximum at $k = 25$ mm^{-1} and $\lambda = 250$ µm, indicating a dominant process of wave propagation.

Furthermore, the high-resolution images obtained in the experiments showed small bubbles in the lamella, which often burst after they reached the middle of the crown. These small bubbles each had an initial diameter of approximately 100 µm, and their bursting processes developed waves that expanded over the lamella (see Fig. 11). We assume that if the lamella is locally thin enough, the bursting of these bubbles produces the holes. Furthermore, analyzing the wave dispersion of the bubbles using the same methods as with the holes, we demonstrate that the wave numbers in the power spectral density correlate with each other, showing the same character (see Fig. 10(c)). This supports our claim that these bubbles are responsible for the hole formation, and it is similar to the conclusions made by Marston et al. (2016).

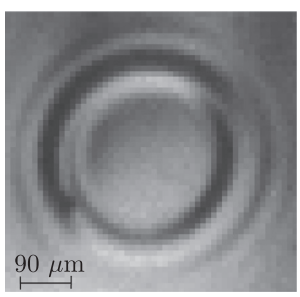

Fig. 11. Wave pattern in the lamella after bubble breakup at $We = 2281$ and $u^* = 0.05$. The waves propagate symmetrically and have the same spectral density as the holes.

4.3. Crown thickness

The presence of these expanding holes allows us to calculate the lamella thickness during splashing. The thickness is obtained by rewriting the Taylor–Culick equation (see Taylor, 1959; Culick, 1960) for wave velocity as

$$h_{lm} = \frac{2\sigma_{l,g}}{\rho_l u_{\text{hole}}^2}, \tag{3}$$

where u_{hole} is the expansion velocity of the holes.

Fig. 12 shows the evolution of the lamella thickness after the breakup process. When the droplets impacted at $We = 2281$, the thickness increased up to $\tau \approx 7.6$ and then remained constant. However, at higher Weber numbers, the thickness varied notably depending on the film velocity. The reason for this is the increase in the number of capillary waves present in the lamella along with the Weber number as can be seen by comparing Figs. 4 and 8. The thickness remained relatively constant and equaled $h_{lm} = 31 \pm 3$ µm for all setups in the latest stage. The total number of videos used for the thickness calculation was only 25 due to the challenging task of capturing one of both lamella sides using a small depth

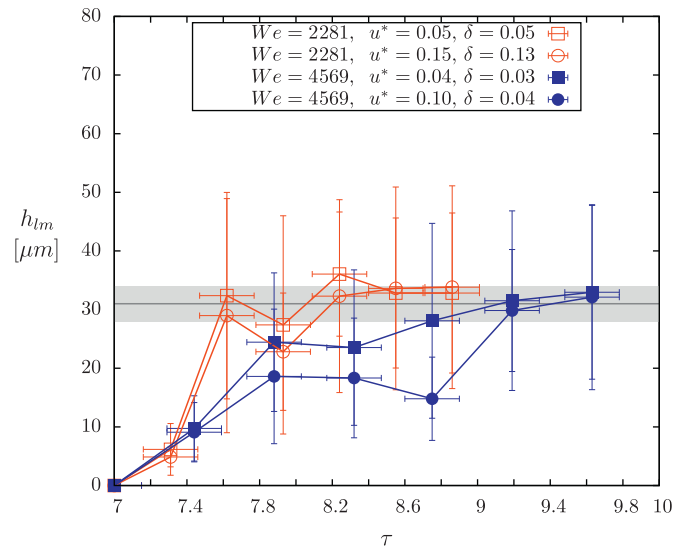

Fig. 12. Lamella thickness as a function of τ. The holes formed first at $\tau = 7 \pm 0.5$ regardless of the experimental setup. A total of 25 images for each case was used to calculate the lamella thickness.

of field of 2 mm. This was necessary to obtain a sharp image of the lamella without any intensity interference from its other side.

To validate the value for lamella thickness obtained by using the Taylor–Culick equation, we benefit from the detected waves (see Fig. 10(a)) and calculate the thickness using the nonlinear theory presented by Prévost and Gallez (1986). In this theoretical investigation on the rupture of free liquid films, the growth rates of the disturbances are estimated as a function of the wave number. Applying this theory yields

$$h_{lm} = \frac{\lambda k_{\max}}{2\pi}, \tag{4}$$

where $k_{\max} = 0.7$ is the dimensionless wave number corresponding to the fastest rate of growth of the disturbances, and λ the related wavelength. Our measurements revealed that the most common wavelength around the holes was of 250 ± 50 µm. Using this information in the nonlinear theory, we obtain a lamella thickness of $h_{lm} = 28 \pm 6$ µm, which provided us a similar thickness to the estimated by the Taylor–Culick analysis.

5. Conclusions

Our experimental investigation showed that the film velocity affects the development of the crown geometry significantly. When the film velocity remained smaller than 5% of the impact velocity, the crown shape was similar to the impact on film layers at rest; however, an increase of the film velocity over 10% of the impact velocity induced a strong curvature on the lamella. This curvature is observed only until $\tau \approx 5$ regardless of the Weber number. Afterwards, the crown shape grew more perpendicular to the film and a symmetrical shape was formed. We quantified those effects on the crown geometry by measuring the crown diameter and height over time, and showed that the diameter decreased and the height increased with the film velocity and thickness in the last phase of splashing $\tau > 5$. Another important effect of the moving film observed in this study was that the fluid flow continuously supplied the crown with liquid, delaying the breakup process.

We detected that the crown completely destroyed itself due to two different types of instabilities, atomizing it into secondary droplets. The first detected instability were holes surrounded by waves, which spread throughout the lamella at $\tau \approx 7 \pm 0.5$ for flow velocities lower than 5% of the impact velocity. For higher film ve-

locities, the breakup process is delayed and the holes are formed at $\tau \approx 8 \pm 0.5$. Afterwards the second instability appeared, separating the crown from the base. We also observed bubbles in the lamella, whose bursts produced similar wave numbers to those of the formed holes. The same character in the power spectral density supports our claim that these bubbles are responsible for the hole formation. One can hypothesize that these bubbles originate from the air entrapped between the droplet and film in the early phase of impact (Tran et al., 2013), however, a high amount of bubbles due to this process have been only observed at low Weber numbers, as shown in Thoroddsen et al. (2012). Despite these discoveries, more experiments and numerical simulations are needed to track the entrapped air under a moving film at high Weber numbers.

Moreover, we calculated the lamella thickness during the splashing using the Taylor–Culick equation and the nonlinear rupture theory. Both methods estimated a dimensional lamella thickness of 31 ± 3 μm for all the studied cases.

Acknowledgments

We are thankful to Deutsche Forschungsgemeinschaft (Project BA 4953-3) for the financial support, and to Ilia Roisman and Cameron Tropea from the Technische Universität Darmstadt for their helpful comments and the loan of the camera.

Supplementary material

Supplementary material associated with this article can be found, in the online version, at 10.1016/j.ijmultiphaseflow.2018.01.015.

References

Alghoul, S., Eastwick, C., Hann, D., 2011. Normal droplet impact on horizontal moving films: an investigation of impact behaviour and regimes. Exp. Fluids 50, 1305–1316.
Bringi, V., Chandrasekar, V., Hubbert, J., 2003. Raindrop size distribution in different climatic regimens from disdrometer and dual-polarized radar analysis. J. Atmos. Sci. 60 (2), 354–365.
Cossali, G., Coghe, A., Marengo, M., 1997. The impact of a single drop on a wetted solid surface. Exp. Fluids 22, 463–472.
Culick, F., 1960. Comments on a ruptured soap film. J. Appl. Phys. 31 (6), 1128–1129.
Deegan, R., Brunet, P., Eggers, J., 2008. Complexities of splashing. Nonlinearity 21, C1–C11.
Dhiman, R., Chandra, S., 2010. Rupture of thin films formed during droplet impact. Proc. R. Soc. A 466, 1229–1245.
EASA, 2009. Certification Specifications for Large Aeroplanes CS-25.
Faßmann, B., 2015. Zeitabhängige charakterisierung der sekundärtropfen aus dem hochgeschwindigkeitsaufprall einzelner flüssigkeitstropfen. Technische Universität Braunschweig Dissertation.
Faßmann, B., Bansmer, S., Moeller, T., Radespiel, R., Hartmann, M., 2013. High velocity impact of single droplets on a dry smooth surface. Exp. Fluids 54, 1516.
Gaylard, A., Duncan, B., 2011. Simulation of rear glass and body side vehicle soiling by road sprays. SAE Int. J. Passenger Cars Mech. Syst. 4, 184–196.
Hammond, D., Quero, M., Ivey, P., 2005. Analysis and experimental aspects of the impact of supercooled water droplets into thin water films. AIAA-2005-77 Reno, Nevada.
Josserand, C., Thoroddsen, S., 2016. Drop impact on a solid surface. Annu. Rev. Fluid Mech. 48, 365–391.
Liu, Y., Chen, W., Bond, L., Hu, H., 2017. An experimental study on the characteristics of wind-driven surface water film flows by using a multi-transducer ultrasonic pulse-echo technique.. Phys. Fluids 29, 012102.
Marston, J., Truscott, T., Speirs, N., Mansoor, M., Thoroddsen, S., 2016. Crown sealing and buckling instability during water entry of spheres. J. Fluid Mech. 794, 506–529.
Opfer, L., Roisman, I., Venzmer, J., Klostermann, M., Tropea, C., 2014. Droplet-air collision dynamics: evolution of the film thickness. Phys. Rev. E 89 (1), 013023.
Pan, K., Cheng, K., Chou, P., Wang, C., 2008. Collision dynamics of high-speed droplets upon layers of variable thickness. Exp. Fluids 45, 435–446.
Prévost, M., Gallez, D., 1986. Nonlinear rupture of thin free liquid films. J. Chem. Phys. 84, 4043.
Rioboo, R., Bauthier, C., Conti, J., Vou, M., De Coninck, J., 2003. Experimental investigation of splash and crow formation during single drop impact on wetted surfaces. Exp. Fluids 35, 648–652.
Roisman, I., Horvat, K., Tropea, C., 2006. Spray impact: rim transverse instability initiating fingering and splash, and description of a secondary spray. Phys. Fluids 18, 102104.
Roisman, I., Tropea, C., 2002. Impact of a drop onto a wetted wall: description of crown formation and propagation. J. Fluid Mech. 472, 373–397.
Taylor, G., 1959. The dynamics of thin sheets of fluid. II. Waves on fluid sheets. Proc. R. Soc. A 253, 296–312.
Thete, S., Anthony, C., Basaran, O., Doshi, P., 2015. Self-similar rupture of thin free films of power-law fluids. Phys. Rev. E 92 (2), 023014.
Thoroddsen, S., 2002. The ejecta sheet generated by the impact of a drop. J. Fluid Mech. 451, 373–381.
Thoroddsen, S., Etoh, T., Takehara, K., 2006. Crown breakup by Marangoni instability. J. Fluid Mech. 557, 63–72.
Thoroddsen, S., Etoh, T., Takehara, K., 2008. High-speed imaging of drops and bubbles. Annu. Rev. Fluid Mech. 40, 257–285.
Thoroddsen, S., Thoraval, M., Takehara, K., Etoh, T., 2012. Micro-bubble morphologies following drop impacts onto a pool surface. J. Fluid Mech. 708, 469–479.
Tran, T., de Maleprade, H., Sun, C., Lohse, D., 2013. Air entrainment during impact of droplets on liquid surfaces. J. Fluid Mech. 726, R3. 10
Wang, A., Chen, C., 2000. Splashing impact of a single drop onto very thin liquid films. Phys. Fluids 12, 2155.
Yarin, A., 2006. Drop impact dynamics: splashing, spreading, receding, bouncing.... Annu. Rev. Fluid Mech. 38, 159–192.
Yarin, A., Weiss, D., 1995. Impact of drops on solid surfaces: self-similar capillary waves, and splashing as a new type of kinematic discontinuity. J. Fluid Mech. 283, 141–173.
Zhang, L., Brunet, P., Eggers, J., Deegan, R., 2010. Wavelength selection in the crown splash. Phys. Fluids 22, 122105.
Zhang, L., Toole, J., Fezzaa, K., Deegan, R., 2012. Evolution of the ejecta sheet from the impact of a drop with a deep pool. J. Fluid Mech. 690, 5–15.

View publication stats